Heat and mass transfer across the vapor–liquid interface: A comparison of molecular dynamics and the Enskog–Vlasov kinetic model

Simon Homes, Aldo Frezzotti, Isabel Nitzke, Henning Struchtrup, and Jadran Vrabec

2025

Faculty of Engineering and Computer Science

Faculty Publications

© 2025 Homes, Frezzotti, Nitzke, Struchtrup, and Vrabec. This is an open access article distributed under the terms of the license Creative Commons License CC BY: http://creativecommons.org/licenses/by/4.0/

Original citation:
Homes, S., Frezzotti, A., Nitzke, I., Struchtrup, H., & Vrabec, J. (2025). Heat and mass transfer across the vapor-liquid interface: A comparison of molecular dynamics and the Enskog-Vlasov kinetic model. *International Journal of Heat and Mass Transfer*, *242*, 126828.
https://doi.org/10.1016/j.ijheatmasstransfer.2025.126828

Downloaded from UVicSpace Research & Learning Repository

dspace.library.uvic.ca

University of Victoria | Libraries

International Journal of Heat and Mass Transfer 242 (2025) 126828

Contents lists available at ScienceDirect

International Journal of Heat and Mass Transfer

journal homepage: www.elsevier.com/locate/hmt

Heat and mass transfer across the vapor–liquid interface: A comparison of molecular dynamics and the Enskog–Vlasov kinetic model

Simon Homes [a], Aldo Frezzotti [b], Isabel Nitzke [a], Henning Struchtrup [c], Jadran Vrabec [a,*]

[a] Thermodynamik, Technische Universität Berlin, 10587 Berlin, Germany
[b] Dipartimento di Scienze e Tecnologie Aerospaziali, Politecnico di Milano, 20133 Milano, Italy
[c] University of Victoria, Victoria, BC V8W 2Y2, Canada

ARTICLE INFO

Dataset link: 10.14279/depositonce-21982

Keywords:
Molecular Dynamics
Direct Simulation Monte Carlo
Lennard-Jones potential
Sutherland potential
Evaporation
Heat flux

ABSTRACT

Due to the intricacies of the interface between vapor and liquid, evaporation and condensation processes are not fully understood. The small spatial extent of the interface renders experimental studies on this subject challenging so that computational investigations are indispensable. For two heat and mass transfer scenarios across a vapor–liquid interface, molecular dynamics simulation is compared with the direct simulation Monte Carlo solution of the Enskog–Vlasov kinetic equation. A heat flux from the vapor to the liquid in a closed system as well as classical evaporation into an open half-space are considered. In both scenarios, temperature and one-dimensional driving gradients are widely varied, sampling systems containing $5 \cdot 10^5$ molecules. Since the two simulation methods rest on different potential models for the molecular interactions, a meaningful transformation between the truncated and shifted Lennard-Jones fluid and the Sutherland fluid is proposed. Spatially resolved density, temperature and velocity profiles from these simulation methods are consistent, except for the interface width. Consequently, particle flux and downstream pressure match as well. The good agreement between the results reinforces the validity of these approaches. The study is accompanied by successful comparisons of these simulations to kinetic gas theory with respect to macroscopic property variations at the interface.

1. Introduction

Evaporation and condensation processes, i.e. phase change between liquid and vapor, are ubiquitous in nature and technical applications. They take place across a phase boundary that is usually addressed as the interface, which complicates these mechanisms. Despite their longstanding investigation, they are not fully understood.

Molecular simulations [1–9] reveal the interface as a region with steep gradients of density and – under non-equilibrium conditions – of temperature, hydrodynamic velocity and other properties. With a thickness that is typically on the order of ten molecular diameters (plus a Knudsen layer that extends over several multiples of the mean free path under non-equilibrium conditions [9]), the interface region is narrow so that it appears as a discrete boundary at resolutions that are typically employed for applications. On this scale, the steep interfacial variations of temperature and velocity reduce to discontinuities, and emerge, e.g., as a temperature jump or velocity slip [10,11]. Hence, from the viewpoint of non-equilibrium applications, well-designed jump and slip conditions are required that connect the Navier–Stokes–Fourier equations for the adjacent phases. These must be constructed such that they reflect the underlying microscopic details of the resolved interface region.

Well-known jump and slip models based on the kinetic gas theory or non-equilibrium thermodynamics rely on phenomenological interface parameters, such as evaporation and condensation coefficients or interface resistivities [10,12–16], which must be determined from experiments or first principles. However, the experimental determination of these parameters is notoriously difficult, with reported values for evaporation and condensation coefficients of, e.g., water varying over three orders of magnitude or more [17,18]. At least in part, this is because pronounced jump effects are expected mainly in microscopic systems, where interface resistivities contribute significantly to the overall resistance to heat and mass transfer [19].

Results from experiments with macroscopic systems published by C.A. Ward and his group since 1999 [20–23] were widely noticed, triggering new interest in research on non-equilibrium phase change. Ward and coworkers measured temperature jumps and deviations from the saturation pressure in forced steady-state evaporation experiments, finding unexpectedly large temperature jumps of up to 7 K (or even

* Corresponding author.
E-mail address: vrabec@tu-berlin.de (J. Vrabec).

https://doi.org/10.1016/j.ijheatmasstransfer.2025.126828
Received 1 November 2024; Received in revised form 17 January 2025; Accepted 12 February 2025
0017-9310/© 2025 The Authors. Published by Elsevier Ltd. This is an open access article under the CC BY license (http://creativecommons.org/licenses/by/4.0/).

larger when the vapor was heated [24]). Measurements of this type are subject to possibly significant errors: Temperature differences are difficult to localize since thermo-couples are much wider than the interface region. Also, pressure deviations from saturation are as large as the experimental error associated with their measurement. A recent detailed assessment of experiments and models [25] shows that this high level of uncertainty renders it impossible to judge competing theories that aim to describe non-equilibrium processes involving interfaces between vapor and liquid phases.

Due to the lack of reliable experimental data, interface parameters must be determined from first principles, either directly, or indirectly from molecular simulations. Indeed, next to the macroscopically observed material behavior that manifests itself in the thermodynamic equilibrium properties and transport coefficients, also the coveted interface resistivities are a consequence of the interactions of the molecules that the given fluid is comprised of [9]. From the viewpoint of classical physics, the behavior of matter is governed only by the mass of molecules and their interactions, which give rise to repulsive and attractive forces. For simple molecules like the noble gases, already two parameters suffice to characterize their interactions, e.g., with the Lennard-Jones (LJ) and Sutherland potentials discussed below.

While an analytical method to determine macroscopic property relations, including interface parameters, from molecular properties alone would be preferable, this is typically not possible due to the complexity of the problem. An alternative are numerical experiments, where atomistic simulations with a sufficiently large number of molecules are carried out to sample the fully resolved bulk liquid and vapor phases together with their connecting interface. The desired macroscopic properties and interface parameters can then be extracted from the results, e.g., by fitting continuum models with jump and slip [4,9].

The determination of interface parameters requires accurate non-equilibrium simulations over a wide range of process parameters. Although several authors have presented related numerical experiments and results [4,9,26,27], these have not yet gelled into a comprehensive understanding of the interface parameters, and their dependence on the local state as well as – possibly – process conditions. Kinetic theory models, which are limited to low pressure, where the vapor behaves as an ideal gas, point to state-dependent evaporation and condensation coefficients, which are expected to depend at least on the temperature of the interface [4,9].

Onsager's reciprocity relations postulate a symmetric resistivity matrix [10,28], at least for linear processes that are not overly far from equilibrium. Typical molecular simulations take place under strong non-equilibrium conditions, induced by large temperature gradients or evaporation mass flows. This is required to distinguish the emerging signals from stochastic fluctuations. While some authors claim symmetry for their results [26], these are not conclusive [29], and more recent results on larger systems clearly give non-symmetric resistivities [9], which might be related to a very strong degree of non-equilibrium [30]. However, it should be noted that experimental conditions are typically much closer to (local) equilibrium and are thus quite different from those in molecular simulations.

To summarize: (a) Interface jump conditions for continuum models require interface resistivities (or evaporation and condensation coefficients) as functions of the local state at the interface. (b) These must be determined with atomistic simulations covering a wide range of conditions from close to far from the critical point, and from weak to strong non-equilibria. This contribution focuses on the second demand.

Molecular modeling and simulation approaches are costly, with higher accuracy requiring larger systems and more computational effort. With that, the desired program of generating simulations over a large range of conditions is challenging. Ideally, several independent approaches would be used to create complementary data, where each is employed in its most suitable range of the simulation space. The focus of this contribution lies on the comparison of two molecular simulation methods, Molecular Dynamics (MD) and the Direct Simulation Monte Carlo (DSMC) solution of the Enskog–Vlasov (EV) kinetic equation [5,7,31,32]. In the following, the latter is referred to as EV-DSMC.

In the model hierarchy addressed above, MD provides the most accurate description of a fluid whose properties are completely defined by the chosen intermolecular potential, without additional assumptions beyond those intrinsic in the numerical integration of Newton's equations of motion for a molecular ensemble. Truncated potentials with a limited interaction range reduce the computational cost so that this work relies on the truncated and shifted Lennard-Jones (LJTS) potential.

The EV model is intrinsically less accurate due to its underlying assumptions. Following Enskog theory of the dense hard-sphere fluid [33], the EV equation forces a fluid, whose atoms interact pairwise via the Sutherland potential [34], to be completely characterized by the one-particle distribution function. Pair correlations are thus described phenomenologically [35]. The addition of intermolecular attractive forces through a Vlasov-like self-consistent force field to the hard-sphere Enskog collision term gives the EV equation the capability to provide a unified description of the liquid and vapor phases, connected by a fully resolved interface [7,31,32].

As MD, EV-DSMC also operates with particles, representing atoms or molecules. For spatially one- or two-dimensional problems, EV-DSMC requires a computational effort per particle that is much smaller than MD to traverse the temporal domain. For three-dimensional problems, however, the computational effort is expected to become comparable, mainly because of the evaluation of the Vlasov term [5,7,36]. Irrespective of computational efficiency, the EV model is useful since, although approximate, it is described by a single kinetic equation. The latter can be exploited not only on the numerical side, but also to obtain analytical results [7,32] as well as hydrodynamic equations [9,37] that help understanding such complex flows. Due to its phenomenological nature, the EV equation model needs to be validated against MD that is free from the assumptions leading to the EV model, extending the successful comparisons between MD and Enskog theory for the hard-sphere fluid [38].

Section 1 introduces the considered simulation scenarios, gives a brief overview of the employed MD and EV-DSMC methods and discusses the choice of potential models that allow for a meaningful comparison. Section 2 presents a detailed comparison of the simulation results for the heat flux scenario and the evaporation scenario. Further, in view of the importance of past kinetic theory studies [39,40], simulation results are compared to ideal gas kinetic theory with respect to the jumps at the interface. Such comparisons are important because the Boltzmann equation [41], governing ideal gas flows, uses phenomenological boundary conditions at the vapor–liquid interface. However, it can describe flows on the scale of the mean free path that are much larger than the molecular size, under ideal gas conditions. MD and EV, with a different accuracy, are complementary to the Boltzmann equation to some extent. MD and EV share the capability of describing the fluid at the scale of the molecular size. Unlike the Boltzmann equation, they can be used to investigate non-ideal vapors in the kinetic regime and to obtain/validate the kinetic boundary conditions for the Boltzmann equation, thanks to their capability of giving a unified description of liquid, interface and vapor. The very same reasons that make MD or EV useful, render them impractical to study flows on a scale that is much larger than the molecular size. Additional results are summarized in the supplementary material. The final section concludes this work.

2. Methods

2.1. Scenarios

Two stationary scenarios were selected to serve as a benchmark for the comparison between MD and EV-DSMC simulations. One scenario imposes a strong heat flux across a vapor–liquid interface without net

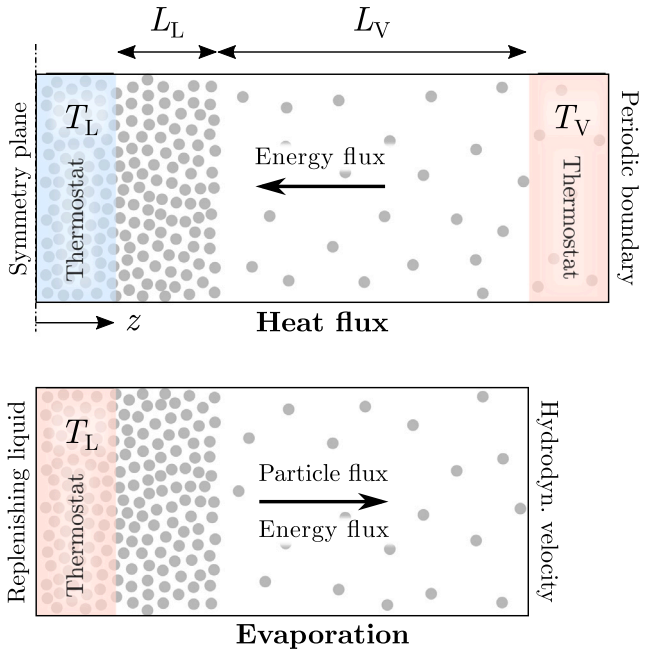

Fig. 1. Schematics of the two test scenarios with their boundary conditions. Molecules are symbolized as gray circles.

particle flux, while the other one considers evaporation. To generate such scenarios, appropriate boundary conditions have to be specified in MD and EV-DSMC, respectively. Different temperatures were considered as well as varying gradients so that a wide parameter range was covered in this comparison.

In the heat flux scenario (see Fig. 1, top), the simulation domain was closed, i.e. the number of molecules remained constant. To invoke and maintain a heat flux from the vapor to the liquid, the central section of the bulk liquid was cooled, while a section of the far field of the bulk vapor was heated.

In the evaporation scenario (see Fig. 1, bottom), the target hydrodynamic velocity near the outer limit of the far field of the vapor was imposed by deleting certain molecules. To maintain stationarity, the liquid was replenished. While the central section of the bulk liquid was thermostated to a constant specified temperature, the rest of the domain was left untouched such that the molecules could move freely. The vapor volume was sufficiently large to accommodate a possible Knudsen layer adjacent to the interface.

2.2. Molecular dynamics

MD treats fluids by mimicking the motion of a set of individual molecules. It assumes that the entire molecular ensemble acts as a mechanical system and follows a trajectory in phase space. The interactions between the molecules are used to calculate the resulting force F on each molecule. Following Newton's law of motion, $F = m\,\ddot{q}$, the acceleration $\ddot{q}$ is related to the force and the molecule's mass m. Since the resulting force on each molecule depends on its position q and the positions of other molecules around it, Newton's law of motion is a coupled second-order differential equation. For more than two molecules in the system, this equation has to be solved numerically by time discretization, which was done in the present work with the software *ls1 mardyn* [42] using a Leapfrog integrator with an appropriate time step that amounted to $\Delta t \approx 2\,\mathrm{fs}$ when assuming potential parameters for argon [43]. Since MD simulation is based on very few model assumptions and is capable of keeping track of each molecule's individual path through space and time, phenomena on the molecular scale can be investigated with great precision and accuracy.

One of the main assumptions of MD is the specification of the interaction potential between the molecules. A good trade-off between predictive power and computational efficiency is given by the LJ potential [44,45], which also defines the force $F = -\partial u_{\mathrm{LJ}}/\partial r$ between two molecules as a function of their distance r

$$u_{\mathrm{LJ}}(r) = 4\varepsilon\left[\left(\frac{\sigma}{r}\right)^{12} - \left(\frac{\sigma}{r}\right)^{6}\right], \tag{1}$$

with the size parameter σ and the energy parameter ε.

The LJ potential was used here in its truncated and shifted form, avoiding long-range corrections, which is beneficial for simulations of heterogeneous systems. Using a cutoff radius of 2.5σ, the LJTS potential is given by

$$u_{\mathrm{LJTS}}(r) = \begin{cases} u_{\mathrm{LJ}}(r) - u_{\mathrm{LJ}}(2.5\sigma), & r \le 2.5\sigma, \\ 0, & r > 2.5\sigma. \end{cases} \tag{2}$$

Numerous studies [46–49] have been carried out with this potential so that its equilibrium properties and transport coefficients are well known, which is a sound basis for the present investigations.

In both scenarios, the number of molecules was approximately $5{\cdot}10^5$ and the production runs were executed for about $5 \cdot 10^6$ time steps under stationary conditions. This allowed to keep the fluctuations low and achieve good statistics. The quantities of interest, e.g., density, temperature and hydrodynamic velocity profiles, were sampled binwise during the production run with a bin width of half a molecule diameter 0.5σ. Both scenarios were initially set up by simulating coexisting liquid and vapor phases in direct physical contact so that a vapor–liquid equilibrium (VLE) evolved. By subsequently applying the boundary conditions described in the following, the two considered scenarios emerged.

In the heat flux scenario, the simulation domain was chosen to be symmetric and composed of a liquid and a vapor phase so that periodic boundary conditions could be invoked in all spatial directions. To generate the heat flux from the vapor to the liquid, two thermostats with a width of 5σ were established in sections of the respective phases. The non-thermostated region had a width of $L_{\mathrm{L}} = 10\sigma$ in the liquid and $L_{\mathrm{V}} = 400\sigma$ in the vapor.

In the evaporation scenario, an algorithm described by Meland et al. [6] that operates by deleting certain molecules was used to specify the target hydrodynamic velocity in the far field of the vapor. The liquid was replenished using a dedicated method [1] to maintain stationarity. Between the thermostat in the bulk liquid and the interface, there was a non-thermostated liquid region of width $L_{\mathrm{L}} = 10\sigma$. The width of the vapor phase without any external interference was chosen to be $L_{\mathrm{V}} = 400\sigma$ so that its geometry was consistent with the other scenario.

2.3. Enskog–Vlasov equation

The EV equation, proposed by De Sobrino in 1967 [31], provides an approximate description of a fluid constituted by monatomic molecules with the mass m that interact pairwise via the Sutherland potential [34]

$$\phi(r) = \begin{cases} \infty & r < \sigma, \\ \phi_t(r) & r \ge \sigma, \end{cases} \tag{3}$$

in which repulsion is described by hard-sphere impulsive forces, whereas attraction is described by the soft tail potential ϕ_t. In Eq. (3), σ is the hard-sphere diameter and r the distance between two molecules.

Following the Enskog theory of the dense hard-sphere fluid [50], a closed equation for the fluid one-particle distribution function [51] is obtained in the unsteady and spatially one-dimensional form

$$\frac{\partial f}{\partial t} + v_z\frac{\partial f}{\partial z} + \frac{F_z(z,t)}{m}\frac{\partial f}{\partial v_z} = C_{\mathrm{hs}}(f,f), \tag{4}$$

where $f(z,\mathbf{v},t)$ is the one-particle distribution function of molecular velocities $\mathbf{v}$ at the spatial position z and time t.

The collision integral $C_{\rm hs}(f,f)$ on the r.h.s. of Eq. (4) gives the rate of change of f due to short-range, repulsive interactions, described as instantaneous, binary elastic collisions between two molecules. At the time of their collision, the spatial positions of the molecules are $\mathbf{r}$ and $\mathbf{r}-\sigma\mathbf{k}$, with $\mathbf{k}$ being a unit vector determining the relative position of the colliding molecules. Each collision changes the velocities of the interaction partners $\mathbf{v}$ and $\mathbf{v}_1$ to their respective post-collision values $\mathbf{v}^*$ and $\mathbf{v}_1^*$

$$\mathbf{v}^* = \mathbf{v} + (\mathbf{k}\cdot\mathbf{v}_r)\mathbf{k}, \quad \mathbf{v}_1^* = \mathbf{v}_1 - (\mathbf{k}\cdot\mathbf{v}_r)\mathbf{k}, \quad \mathbf{v}_r = \mathbf{v}_1 - \mathbf{v}. \tag{5}$$

Within the framework of the Standard Enskog Theory [52], $C_{\rm hs}(f,f)$ takes the form

$$C_{\rm hs}(f,f) = \sigma^2 \int_S \Big[\chi_{\rm hs}(z, z+\sigma k_z) f(z+\sigma k_z, \mathbf{v}_1^*, t) f(z, \mathbf{v}^*, t) - \chi_{\rm hs}(z, z-\sigma k_z) f(z-\sigma k_z, \mathbf{v}_1, t) f(z, \mathbf{v}, t) \Big] (\mathbf{v}_r\cdot\mathbf{k})^+ d\mathbf{v}_1 d^2\mathbf{k}, \tag{6}$$

where $\chi_{\rm hs}$ is the uniform equilibrium pair correlation function at contact [51] and the superscript + indicates that the surface integral is restricted to the half-sphere for which $(\mathbf{v}_r\cdot\mathbf{k})>0$. $\chi_{\rm hs}$ is a function of the local number density $n(z)$ and is often approximated as

$$\chi_{\rm hs}(\mathbf{r}, \mathbf{r}\pm\sigma\mathbf{k}) = Y\left(n\left[\mathbf{r}\pm\sigma\frac{\mathbf{k}}{2}\right]\right), \quad Y(n) = \frac{1}{2}\frac{2-\xi}{(1-\xi)^3}, \quad \xi = \frac{\pi n}{6}\sigma^3, \tag{7}$$

using the relation between Y and the equation of state of the hard-sphere fluid [51], which is well described by the Carnahan–Starling equation [53].

The z component of the Vlasov self-consistent force field $F_z(z,t)$ describes the total action of attractive forces on a molecule at spatial position z and time t. Neglecting spatial correlations, elementary calculations show that in the one-dimensional slab geometry considered here, this attractive force is [7,32]

$$F_z(z,t) = -2\pi \left[\phi_t(\sigma) \int_{|y-z|\le\sigma} (y-z)\, n(y,t)\, dy + \int_{|y-z|>\sigma} (y-z)\, \phi_t(|y-z|)\, n(y,t)\, dy \right]. \tag{8}$$

The soft tail potential ϕ_t affects the thermodynamic properties of the fluid described by Eq. (4) [7,8]. It is easily shown that the equation of state of the Sutherland fluid has the form of a generalized van der Waals equation [54]. Its critical temperature T_c depends on the assumed tail potential ϕ_t, whereas the critical number density n_c is determined only by the hard-sphere diameter [8]. In this work, an algebraic tail of the form

$$\phi_t(r) = -\varepsilon\left(\frac{\sigma}{r}\right)^6, \tag{9}$$

with the minimum of the potential well ε was used. The exponent 6 was chosen to mimic the attractive contribution of the LJ potential [44,45]. The critical parameters for this particular form of the Sutherland potential are [7]

$$\xi_c = \frac{\pi n_c}{6}\sigma^3 = 0.13044\ \sigma^3, \quad T_c = \frac{\varepsilon}{k_{\rm B}}\frac{8}{10.601}, \tag{10}$$

For a temperature $T_0 < T_c$, Eq. (4) admits equilibrium solutions (subscript 0) of the form

$$f_0(z,\mathbf{v}) = \frac{n_0(z)}{(2\pi RT_0)^{3/2}} \exp\left(-\frac{\mathbf{v}^2}{2RT_0}\right), \tag{11}$$

with the gas constant $R = k_{\rm B}/m$ and the Boltzmann constant $k_{\rm B}$. The non-uniform density of the two-phase fluid obeys the equation [7]

$$k_B T_0 \frac{dn_0}{dz} = n_0(z) F_0(z) + 2\pi\sigma^2 n_0(z) k_B T_0 \int_{-1}^{+1} k_z Y\left(n_0\left(z-\sigma\frac{k_z}{2}\right)\right) n_0(z-\sigma k_z)\, dk_z, \tag{12}$$

where $F_0(z)$ is determined by $n_0(z)$ through Eq. (8).

2.4. Direct simulation Monte Carlo solution of the Enskog–Vlasov equation

Eq. (4) can be solved numerically by the extension of the well-known DSMC particle scheme to the dense hard-sphere fluid [5,7], originally formulated by G. A. Bird [55] for the Boltzmann equation of the ideal gas. In the particular implementation of the particle scheme adopted here, a liquid slab occupied the central region of a volume delimited by two identical parallel solid walls. The two symmetrically disposed regions between each interface and its adjacent wall had a nominal width $L_{\rm V}$ and were occupied by the vapor phase. The central section of the liquid slab was kept at the temperature $T_{\rm L}$ with a Berendsen thermostat [56], whereas both solid walls were assigned with the temperature $T_{\rm W} = T_{\rm V}$. The computational domain, whose right half in space $z \ge 0$ is depicted in Fig. 1 (top), was specularly symmetric with respect to the plane located in the center of the liquid slab. Duplicating the spatial domain doubles the computational effort, but avoids the specification of boundary conditions in the center of the liquid slab and reduces the statistical noise associated with Monte Carlo sampling of fluid properties.

At the wall positions, the boundary conditions for the distribution function $f(z,\mathbf{v},t)$ were specified by

$$f(z_{\rm W}^-,\mathbf{v},t) = \frac{n_{\rm W}^-(t)}{(2\pi RT_{\rm W})^{3/2}} \exp\left(-\frac{\mathbf{v}^2}{2RT_{\rm W}}\right), \quad v_1>0,$$
$$f(z_{\rm W}^+,\mathbf{v},t) = \frac{n_{\rm W}^+(t)}{(2\pi RT_{\rm W})^{3/2}} \exp\left(-\frac{\mathbf{v}^2}{2RT_{\rm W}}\right), \quad v_1<0, \tag{13}$$

with wall densities $n_{\rm W}^\pm(t)$ specified according to the flux of impinging molecules on each wall

$$n_{\rm W}^\pm\sqrt{\frac{RT_{\rm W}}{2\pi}} = (1-P_{\rm abs}) \int_{\mathbf{v}\cdot\mathbf{z}^\pm>0} (\mathbf{v}\cdot\mathbf{z}^\pm)\, f(z_{\rm W}^\pm,\mathbf{v},t)\, d\mathbf{v}, \quad \mathbf{z}^\pm = \mp\mathbf{z}, \tag{14}$$

and the unit vector $\mathbf{z}$ associated with the coordinate z.

The boundary conditions (13) and (14) specified that vapor phase molecules hitting any of the walls were either absorbed (with a probability $P_{\rm abs}$) or instantaneously reflected into the domain (with a probability $1-P_{\rm abs}$) and thermalized to $T_{\rm W}$.

Under the present stationarity conditions, the two parameters $T_{\rm W}$ and $P_{\rm abs}$ determine the heat and mass fluxes. For the heat flux scenario, $P_{\rm abs}$ was set to zero so that the walls became impermeable and the net mass flux was zero. In this case, $T_{\rm W}$, together with the bulk liquid temperature $T_{\rm L}$, determined the temperature profile and the heat flux. In the evaporation scenario, the temperature gradient in the downstream equilibrium flow is zero and, as shown by several theoretical and numerical investigations [39,40,57], the downstream equilibrium density and temperature are determined by a single parameter which may either be the mass flux or the downstream Mach number. In this case, it was necessary to tune both $T_{\rm W}$ and $P_{\rm abs}$ to obtain the desired mass flux and a flat downstream temperature profile [9]. Absorbed molecules were re-inserted into the thermostated section of the liquid, after sampling their velocities from a Maxwellian at the temperature $T_{\rm L}$. Results were obtained by the combined time and phase average of 20 statistically independent runs, each considering $4\cdot10^5$ molecules.

2.5. Potential models

Due to the different nature of the LJTS and Sutherland potentials, their properties, e.g., the critical temperature, differ. To allow for a meaningful comparison between simulation results obtained with MD on the basis of the LJTS potential and those obtained with EV-DSMC on the basis of the Sutherland potential, a transformation between LJTS data and Sutherland data was needed. This transformation allows for a

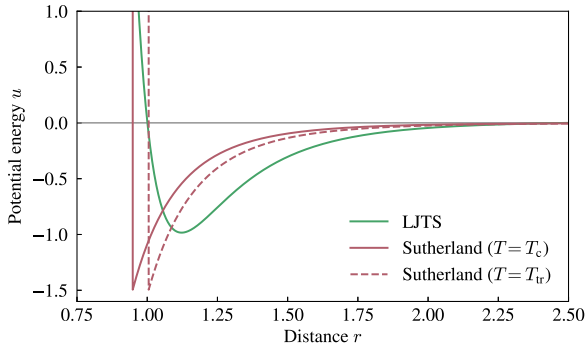

Fig. 2. Potential energy u according to the LJTS potential and the Sutherland potential in LJTS space. The temperature dependence of the size parameter of the Sutherland potential leads to a horizontal shift, depicted for the triple-point temperature T_{tr} and the critical temperature T_c.

joint assessment of key thermodynamic properties that provide insights into the similarities and differences between the two potential models. Thermodynamic properties in LJTS units x can be transformed to units in the Sutherland space x^S using the parameters σ, ε and m (see Table 1).

Since a successful replication of VLE data by a potential model indicates its ability to capture the fundamental thermodynamic characteristics of a fluid in the present scenarios, the conversion of the size parameter σ and energy parameter ε followed the objective to optimize the agreement of the vapor pressure and the saturated liquid density of the LJTS fluid and the Sutherland fluid, with the former being transformed into the Sutherland space. In the relevant temperature range, the Barker–Henderson diameter depends approximately linearly on the temperature [58] so that σ was modeled as a linear function of T. For the LJTS potential, expressions for vapor pressure p_s and saturated liquid density ρ_l were taken from Ref. [46], while the Sutherland data arose from the EV equilibrium obeying Maxwell's equal area rule [37].

VLE data of the LJTS and Sutherland fluids are depicted in Fig. 3. Although the linear temperature dependence of σ fails to capture the shape of the binodal in the critical regime, a satisfying agreement of vapor pressure and saturated densities with deviations below 2% was achieved up to 80% of the critical temperature. A comparison of the resulting enthalpy and entropy under saturation conditions is provided in the supplementary material.

The mass parameter m is only relevant for the transport coefficients. Hence, the thermal conductivity λ and the shear viscosity η were considered for this transformation. Expressions for both quantities were provided by Lautenschläger and Hasse [49] for the LJTS fluid and by Struchtrup et al. [9] for the Sutherland fluid. The adjustment of the mass parameter led to a relatively good agreement of the thermal conductivity of the liquid, but larger deviations arose for the shear viscosity, see supplementary material.

In summary, the obtained Sutherland potential parameters are

$$\begin{aligned} \sigma &= 1.08161672 - 0.12344852\,T\,, \\ \varepsilon &= 1.49580967\,, \\ m &= 0.82866477\,. \end{aligned} \tag{15}$$

Consequently, the parameters of the transformed LJTS potential in Sutherland space are given by the inverse of Eq. (15), namely the temperature-dependent size parameter $\sigma^S = (1.08161672 - 0.12344852\,T)^{-1}$, energy parameter $\varepsilon^S = 0.6685342$ and mass $m^S = 1.2067606$. The behavior of the two potentials in LJTS space is illustrated in Fig. 2. For the sub-critical fluid states considered in this work, the transformed Sutherland potential arises from a horizontal shift in the range between the two depicted potentials, which correspond to the triple-point temperature $T_{tr} = 0.62$ and the critical temperature $T_c = 1.08$ of the LJTS fluid according to Ref. [46].

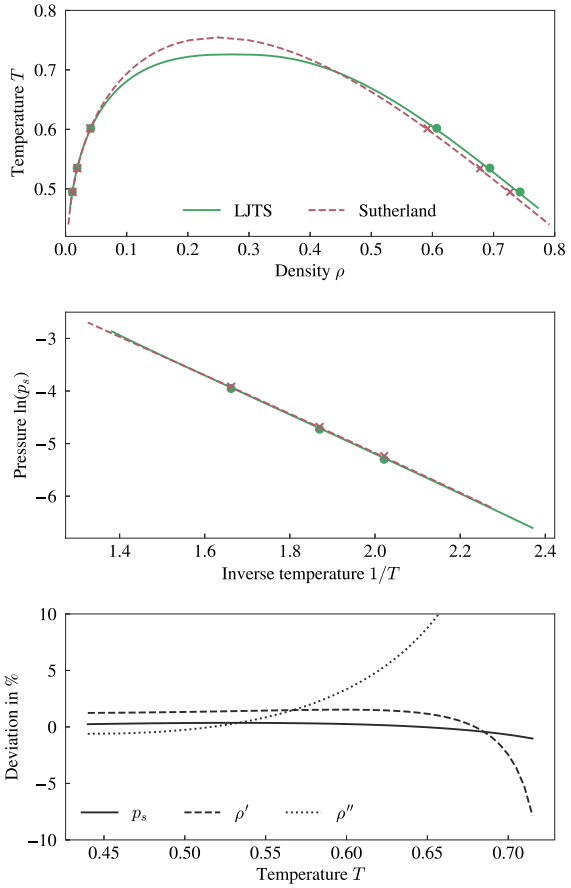

Fig. 3. Saturated densities ρ' and ρ'' (top) and vapor pressure p_s (center) of the LJTS fluid and the Sutherland fluid as well as their relative deviations (bottom). All properties are given in Sutherland space units.

Table 1
Overview of the transformation of LJTS properties into Sutherland space (superscript S).

Property	Transformation
length	$z^S = z/\sigma$
time	$t^S = t\sqrt{\varepsilon/m}/\sigma$
temperature	$T^S = T/\varepsilon$
density (molar)	$\rho^S = \rho\sigma^3$
pressure	$p^S = p\sigma^3/\varepsilon$
enthalpy (molar)	$h^S = h/\varepsilon$
chemical potential (molar)	$\mu^S = \mu/\varepsilon$
thermal conductivity	$\lambda^S = \lambda\sigma^2\sqrt{m/\varepsilon}$
shear viscosity	$\eta^S = \eta\sigma^2/\sqrt{m\varepsilon}$
particle flux (molar)	$j_p^S = j_p\sigma^3\sqrt{m/\varepsilon}$
energy flux	$j_e^S = j_e\sigma^3\sqrt{m/\varepsilon}/\varepsilon$
heat flux	$q^S = q\sigma^3\sqrt{m/\varepsilon}/\varepsilon$

3. Results

Simulations under the same boundary conditions were conducted for both scenarios with MD and EV-DSMC. In the heat flux scenario, three bulk liquid temperatures were considered, while the temperature gradient between liquid and vapor was varied. In the evaporation scenario, also three bulk liquid temperatures were considered and the hydrodynamic velocity in the far field of the vapor was varied. The numerical values of all quantities in this section are discussed in Sutherland space. However, for the sake of brevity, the superscript S is omitted.

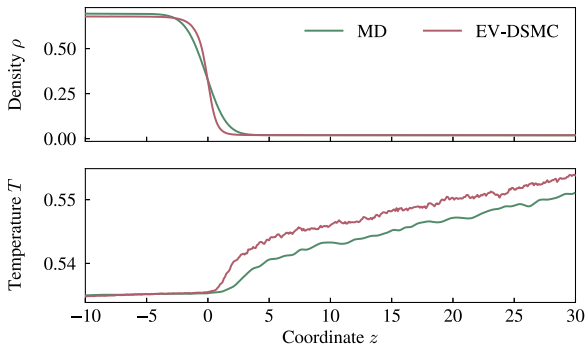

Fig. 4. Density ρ and temperature T as a function of the spatial coordinate z from one simulation run with MD and EV-DSMC, respectively, of the heat flux scenario with a bulk liquid temperature $T_L = 0.5348$ and a target temperature gradient $\Delta T/\Delta z = 0.4 \cdot 10^{-3}$.

3.1. Heat flux scenario

Density and temperature profiles from MD and EV-DSMC in the heat flux scenario are depicted in Fig. 4 for exemplary simulations under the same boundary conditions. From the density profiles, the liquid, vapor and interface can be clearly identified. The sampled density profiles obtained with the two simulation methods show a good agreement in the vapor and liquid. However, the interface thickness calculated by EV-DSMC is smaller than the one obtained from MD. This deviation of the density profile from EV-DSMC can be observed for all present cases in the heat flux scenario (see supplementary material) and can be ascribed to the differences between the LJTS and Sutherland potentials. It should be noted that the interface thickness was not considered in the potential parameter transformation.

The temperature profiles from MD and EV-DSMC agree well for the case depicted in Fig. 4. While they match almost perfectly in the liquid, there are deviations in the vapor that are the consequence of the mismatch at the interface. The different interface thickness shifts the vapor temperature profile from EV-DSMC in positive z direction. Disregarding this shift, it can be seen that the slope of both temperature profiles agrees well in the vapor phase. This deviation is visually magnified by the relatively small gradients and fluxes in this scenario compared to evaporation. Cases with other boundary conditions, i.e. bulk liquid temperature and temperature gradient, are provided in the supplementary material. For a higher bulk liquid temperature and smaller gradients, a better agreement between MD and EV-DSMC in the interface region and vapor phase was found.

Fig. 5 (top) shows the pressure in the far field of the vapor p_∞ as a function of the temperature gradient between liquid and vapor $\Delta T/\Delta z$. While the temperature gradients from MD and EV-DSMC differ, the sampled pressure agrees well. The deviation of the temperature gradients can be explained to some extent by the diverging interface thickness. Further, the gradients in this scenario are rather small compared to evaporation so that the pressure p_∞ mainly depends on the bulk liquid temperature and the temperature gradient has little influence. Hence, p_∞ approximately corresponds to the saturation vapor pressure p_s under VLE conditions ($\Delta T/\Delta z = 0$).

3.2. Evaporation scenario

Density, temperature and velocity profiles of simulations sampled with MD and EV-DMSC under the same boundary conditions are shown in Fig. 6. Even though MD and EV-DSMC show an overall good agreement for the liquid and vapor densities, the thickness of the interface differs, which was also observed in the heat flux scenario. This mismatch of the density profiles in the interface region is not only present in the case shown in Fig. 6, but was observed throughout. Similar to the density profile, the temperature and hydrodynamic velocity profiles

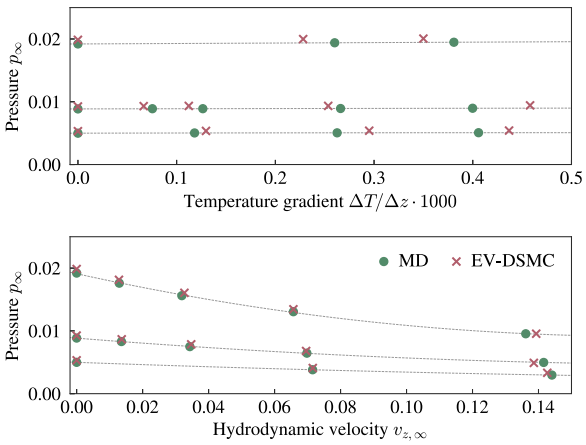

Fig. 5. Pressure in the far field of the vapor p_∞ as a function of the temperature gradient $\Delta T/\Delta z$ in the heat flux scenario (top) and the hydrodynamic velocity in the far field of the vapor $v_{z,\infty}$ in the evaporation scenario (bottom). The dashed lines are a guide to the eye and connect simulations with the same bulk liquid temperature T_L.

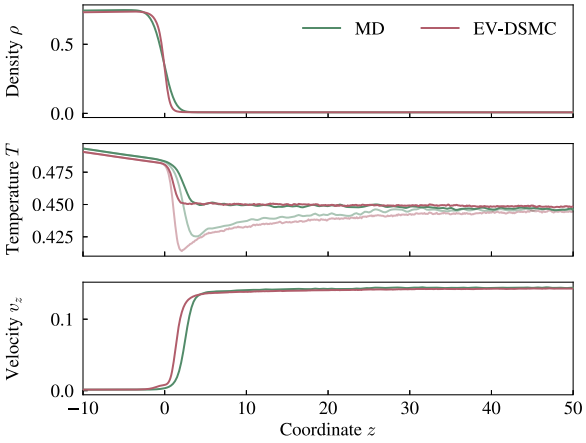

Fig. 6. Density ρ, temperature T and hydrodynamic velocity v_z as a function of the spatial coordinate z from one simulation run with MD and EV-DSMC, respectively, of the evaporation scenario with a bulk liquid temperature $T_L = 0.4947$ and a hydrodynamic velocity in the far field of the vapor $v_{z,\infty} = 0.144$. The faint lines in the center panel show the kinetic temperature in z direction.

agree well in the liquid and vapor phases. However, the steep gradients of temperature and hydrodynamic velocity at the interface are slightly shifted toward the liquid in the EV-DSMC simulations. This effect is independent of the bulk liquid temperature or the hydrodynamic velocity in the far field of the vapor. The second panel of Fig. 6 also shows the component of the kinetic temperature in the downstream direction z. The divergence between this component of the kinetic temperature and the total temperature underlines the strong non-equilibrium character of this evaporation process. Both simulation methods show a qualitatively good agreement, even though the kinetic temperature profile from EV-DSMC exhibits a larger jump at the interface. This effect is present in all evaporation cases, independent of bulk liquid temperature or hydrodynamic velocity in the far field of the vapor.

Fig. 5 (bottom) depicts the pressure p_∞ as a function of the hydrodynamic velocity $v_{z,\infty}$, both sampled in the far field of the vapor. For all three bulk liquid temperatures, the agreement between the results of MD and EV-DSMC is satisfying. Except for small deviations at the highest values, the sampled hydrodynamic velocity in the far field is consistent. However, it can be seen that there is a systematic offset of the pressure in the far field of the vapor. The values from EV-DSMC are almost always about 5% larger than those from MD.

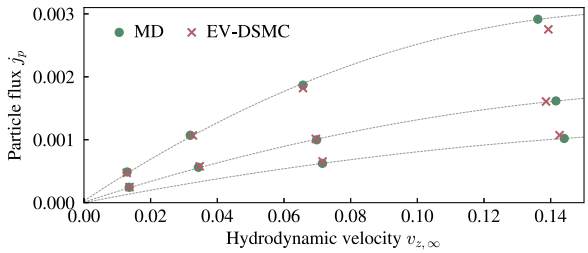

Fig. 7. Particle flux j_p as a function of the hydrodynamic velocity in the far field of the vapor $v_{z,\infty}$ of all simulations in the evaporation scenario. The dashed lines are a guide to the eye and connect simulations with the same bulk liquid temperature T_L.

Fig. 7 shows the particle flux j_p as a function of the hydrodynamic velocity in the far field of the vapor $v_{z,\infty}$ for the simulations in the evaporation scenario. Since there is no particle flux under VLE conditions, all three lines, which connect simulations with the same bulk liquid temperature, have to intersect at the origin. It can be seen that MD and EV-DSMC yield a very similar particle flux under the same boundary conditions. Since the particle flux j_p is given by the product of hydrodynamic velocity v_z and density ρ, i.e. $j_p = v_z\rho$, also the density must agree well. This is confirmed by the findings in Fig. 6. Minor deviations of the resulting particle flux between MD and EV-DSMC were found for a high bulk liquid temperature and a large hydrodynamic velocity in the far field of the vapor.

3.3. Jumps due to heat flux and evaporation

The detailed comparisons between MD and EV-DSMC simulations are completed in this section by a companion analysis of the jumps that the hydrodynamic quantities exhibit across the interface and the nearby Knudsen layer. Characterizing these jumps, for instance through resistivities [4,9,30], allows for connecting the hydrodynamic regions of liquid and vapor by simple relations, which take the presence of the interface and Knudsen layer into account. The MD and EV-DSMC simulations in the evaporation scenario were used to obtain density and temperature jumps across the Knudsen layer, developed by the vapor expansion [40,59]. Temperature jumps caused by a temperature gradient arose from the heat flux scenario. For both scenarios, particular attention was devoted to highlighting possible non-ideal gas effects by contrasting MD and EV-DSMC jumps with the results of the kinetic theory of ideal gases.

The latter was applied only to the vapor region by solving the Boltzmann equation [41]. Coupling with the liquid phase was strongly simplified by assuming a sharp, structureless and planar interface, where the following boundary condition for the distribution function f was assigned

$$v_z f(\mathbf{v}) = v_z f_e(\mathbf{v}) + \int_{v_z'<0} K_s(\mathbf{v}|\mathbf{v}')|v_z'|f(\mathbf{v}')\,d\mathbf{v}' \quad v_z > 0. \tag{16}$$

Eq. (16) states that the flux entering the vapor domain from the interface results from the superposition of two terms. The first one, represented by the distribution function f_e, arises from the molecules that spontaneously evaporate from the liquid bulk. The second term consists of the molecules that are initially impinging on the interface with velocity $\mathbf{v}'$ and are scattered back to the vapor with velocity $\mathbf{v}$, after interacting with the liquid for a time that is much shorter than the vapor mean free time. This assumed instantaneous scattering process is formally described by the time-independent kernel $K_s(\mathbf{v}|\mathbf{v}')$ [41]. The standard choice for modeling the vapor–liquid interaction within the general framework of Eq. (16) is to assume the following Maxwellian form for f_e

$$f_e(\mathbf{v}) = \sigma_e f_{eq}(\mathbf{v}), \quad f_{eq}(\mathbf{v}) = \frac{\rho''(T_\mathrm{I})}{(2\pi R T_\mathrm{I})^{3/2}} \exp\left(-\frac{\mathbf{v}^2}{2k_\mathrm{B}T_\mathrm{I}}\right). \tag{17}$$

Therein, T_I is the liquid temperature at the interface, whereas $\rho''(T_\mathrm{I})$ is the saturated vapor density at T_I. These expressions assume that the equilibrium Maxwellian f_{eq} has no hydrodynamic velocity and is solely characterized by T_I and $\rho''(T_\mathrm{I})$. The velocity-independent evaporation coefficient σ_e accounts for the deviation of the spontaneous evaporation rate from its nominal value.

The associated scattering kernel K_s is usually written in the form

$$K_s(\mathbf{v}|\mathbf{v}_1) = (1-\sigma_e)\left\{\frac{\alpha}{2\pi(k_\mathrm{B}T_\mathrm{L})^2}\exp\left(-\frac{\mathbf{v}^2}{2k_\mathrm{B}T_\mathrm{L}}\right) + (1-\alpha)\,\delta(\mathbf{v}-\mathbf{v}_1+2[\mathbf{v}_1\cdot\mathbf{z}]\mathbf{z})\right\}, \tag{18}$$

with the velocity-independent accommodation coefficient α and the Dirac delta function δ. According to Maxwell's gas-surface scattering model [41], $\alpha = 0$ leads to specular reflection only, while for $\alpha = 1$ there is just diffuse scattering.

The model boundary condition expressed by Eqs. (16) to (18) corresponds to the simplest and, by far, most popular choice to simplify the complexities of molecular scattering from liquid interfaces, but other phenomenological models have been proposed [60,61].

3.3.1. Temperature jump in the heat flux scenario

The temperature profiles in the vapor phase were further analyzed in the framework of the kinetic theory of ideal gases, described by the Boltzmann equation [41]. In this context, temperature jumps across condensed phase boundaries toward a gas have received considerable attention [62]. Therefore, it is of interest to compare the present MD and EV-DSMC vapor temperature profiles with ideal gas results, based on the phenomenological boundary condition given by Eq. (16). For each case simulated with MD and EV-DSMC, a companion DSMC simulation of the vapor phase was made, based on the Boltzmann equation for the ideal hard-sphere gas. As usual [55], reference values of the hard-sphere diameter or mean free path λ_ref were obtained from the shear viscosity η by

$$\lambda_\mathrm{ref} = \frac{16}{5\sqrt{2\pi}}\frac{\eta(T_\mathrm{I},\rho''(T_\mathrm{I}))}{\rho''(T_\mathrm{I})\sqrt{T_\mathrm{I}}}. \tag{19}$$

The above relation is exact for the ideal hard-sphere gas, but provides only a formal, yet useful, definition of the mean free path for other interactions or under non-ideal gas conditions. It should also be noted that the comparison of ideal hard-sphere simulations poses fewer problems in the case of EV-DSMC results since the self-consistent field is negligible in the vapor phase and the hard-sphere interactions dominate. The shear viscosity of the LJTS fluid has a different dependence on temperature and density, and using Eq. (19) only allows matching the shear viscosity of the hard-sphere gas to that of the LJTS fluid at the specified reference values, i.e. $T = T_\mathrm{I}$ and $\rho = \rho''(T_\mathrm{I})$. However, in all considered cases, both temperature and density exhibit small deviations from the respective reference values so that the effective λ_ref can be considered as representative for the entire gaseous flow field.

When pairing ideal gas simulations with EV-DSMC, λ_ref is computed from the shear viscosity of the dense hard-sphere fluid η_hs, as given by the following expression [51]

$$\eta_\mathrm{hs}(\rho,T) = \frac{\eta_0(T)}{Y(n)}\left[1+\frac{4}{5}y+\left(\frac{4}{25}+\frac{48}{25\pi}\right)y^2\right], \tag{20}$$

with the shear viscosity of the ideal hard-sphere gas [63] $\eta_0(T)$ and $y = 4\xi Y(n)$. For LJTS-related simulations, the shear viscosity from Ref. [64] was used.

Fig. 8 shows λ_ref as a function of temperature along the saturated vapor line of the LJTS and Sutherland fluids. λ_ref was computed from the ideal gas limit of the shear viscosity as well as from expressions that take the density dependence into account. The differences are rather small for both fluid models. Fig. 8 shows the mean free path normalized with the respective size parameter σ. A large value indicates a dilute fluid, where only few interactions occur through binary collisions. A

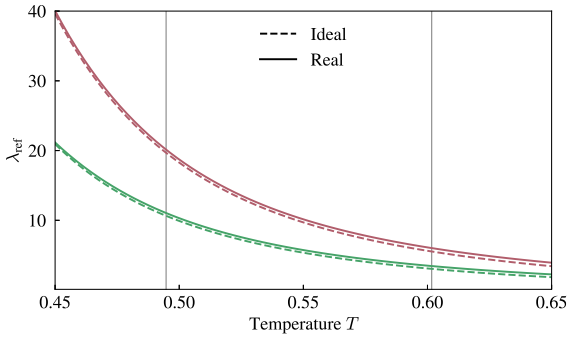

Fig. 8. Effective reference mean free path λ_{ref} in the saturated vapor phase as a function of temperature T for the Sutherland fluid (red) and the LJTS fluid (green). Vertical lines delimit the temperature range of the present simulations. (For interpretation of the references to color in this figure legend, the reader is referred to the web version of this article.)

small value indicates that the mean free path is on the order of the molecular size and the fluid is then dense and non-ideal.

For the ideal gas simulations, the computational domain was bounded by two planar surfaces, located at $z = z_I$ and $z = z_W$, with the spatial width $L_V = z_W - z_I$ of the simulation domain. The boundary condition (16) was applied at $z = z_I$ to mimic the presence of the vapor–liquid interface, which is at the position of the maximum slope of the density profile. Similarly, the temperature T_I in Eq. (16) was set to $T(z_I)$. As shown in Refs. [7,65], this choice allows for a good match between the results of MD/EV and kinetic theory. The required temperature gradient in the vapor phase was imposed by specifying T_W in the thermal wall condition (14) at $z = z_W$, with $P_{abs} = 0$. At least $5 \cdot 10^5$ molecules were used and the kinetic boundary condition (13) was applied at the nominal vapor–liquid interface position $z = 0$. The evaporation coefficient σ_e was set to unity.

The resulting temperature profiles from those DSMC simulations are shown in Fig. 9 along with a comparison to EV-DSMC. For the lowest bulk liquid temperature (bottom), the vapor can be considered as almost ideal, since λ_{ref} is about 19.4, i.e., much larger than the molecular hard-sphere diameter. The profiles exhibit a smooth transition from the liquid to the vapor phase across the interface. Following the transition, the vapor phase emerges where the temperature gradient is fairly constant because of the small temperature variation across the domain. In the EV-DSMC simulations, the region extends up to a distance on the order of λ_{ref} from the thermal wall. The temperature gradient was estimated by simple regression methods and the obtained value was taken for the associated ideal gas simulations by adjusting the temperature T_W.

The temperature profiles in the vapor obtained by the accompanying ideal gas simulations cannot describe the temperature variation within the interface, but they are in excellent agreement with the EV-DSMC profiles in the vapor phase. In these particular cases, EV-DSMC is simulating a nearly ideal hard-sphere vapor so that there is a good match with the Boltzmann-based hard-sphere simulations. However, it is not trivial that the imposed phenomenological boundary condition at the virtual vapor–liquid interface would yield the correct EV temperature jumps.

For the intermediate bulk liquid temperature $T_L = 0.5349$, the reference mean free path λ_{ref} is about 11.3, indicating a weakly non-ideal vapor. This is confirmed by its compressibility at the interface temperature $Z(T_I) = 0.89$, which is the ratio of real to ideal pressure. Also in these cases, ideal gas simulations reproduce the EV-DSMC results quite well, cf. Fig. 9 (center). For the highest bulk liquid temperature, the reference mean free path λ_{ref} was around 5.2, whereas the compressibility $Z(T_I)$ dropped to about 0.806. As Fig. 9 (top) shows, the overall agreement between EV-DSMC temperature profiles and their associated ideal gas profiles is again good, although the ideal gas

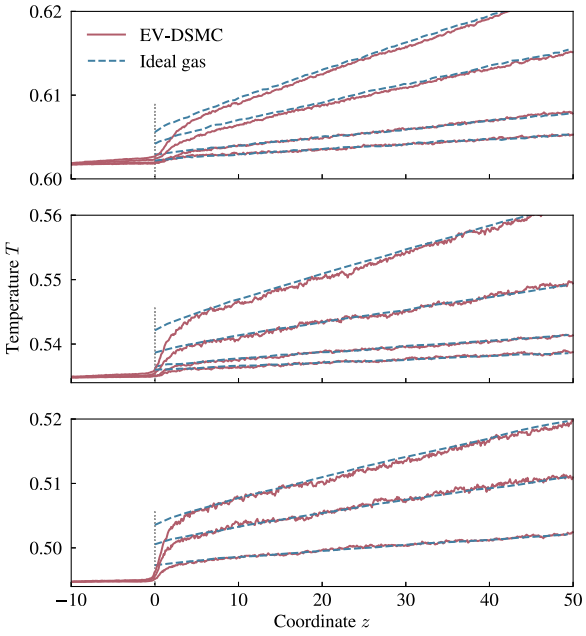

Fig. 9. Comparison of vapor temperature profiles from EV-DSMC and ideal gas simulations in the heat flux scenario. The vertical lines indicate the position of the vapor–liquid interface.

simulation slightly overestimates the EV-DSMC temperature jump when the gradient takes its largest value.

A similar comparison with ideal gas profiles was conducted for the MD simulations, cf. Fig. 10. Note that the reference mean free path of the LJTS fluid is about half of the corresponding Sutherland value, which is a consequence of the different shear viscosity, cf. Fig. 8. The LJTS vapor phase is therefore less ideal, which is confirmed by the slightly lower compressibility $Z(T_I)$ over the entire investigated temperature range, see supplementary material. For the lowest bulk liquid temperature, the agreement between the respective MD and ideal gas profiles is rather good. The same holds for the bulk liquid temperature $T_L = 0.5349$, except for one case, where the ideal profile overestimates the MD data. The temperature gradient does not seem to play a role in this discrepancy, which is likely caused by uncertainties in the temperature gradient estimation. For the highest bulk liquid temperature, the agreement of the temperature profiles is worse than for lower bulk liquid temperatures, since it seems that the ideal profiles overestimate those from MD. Furthermore, the discrepancy increases with a rising temperature gradient.

3.3.2. Density and temperature jumps in the evaporation scenario

Fig. 11 shows the normalized density and temperature jumps from MD and EV-DSMC simulations for a varying downstream Mach number M_∞ and varying bulk liquid temperature T_L to obtain an increasingly non-ideal vapor in the downstream flow. The far-field vapor density ρ_∞ and temperature T_∞ were normalized with the saturated vapor density at the interface temperature $\rho''(T_I)$ and the interface temperature T_I, respectively. The Mach number was computed from the non-ideal speed of sound of the LJTS [48] and Sutherland fluids.

MD and EV-DSMC jumps were compared with the following analytical expressions obtained by Ytrehus [40] and generalized by Cercignani [59] for an evaporation coefficient of unity, which simplify in the present case of a monatomic fluid to

$$\frac{T_\infty}{T_I} = \left(\sqrt{\frac{\pi S_\infty^2}{64} + 1} - \frac{\sqrt{\pi}\, S_\infty}{8} \right)^2, \tag{21}$$

$$\frac{\rho''(T_I)}{\rho_\infty} = \frac{T_\infty}{T_I} \frac{2 \exp\left(-S_\infty^2\right)}{F(S_\infty) + G(S_\infty)\sqrt{T_\infty / T_I}}. \tag{22}$$

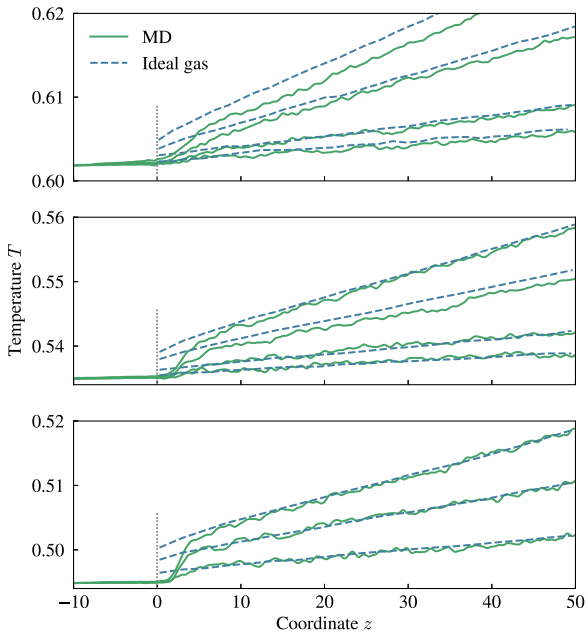

Fig. 10. Comparison of vapor temperature profiles from MD and ideal gas simulations in the heat flux scenario. The vertical lines indicate the position of the vapor–liquid interface.

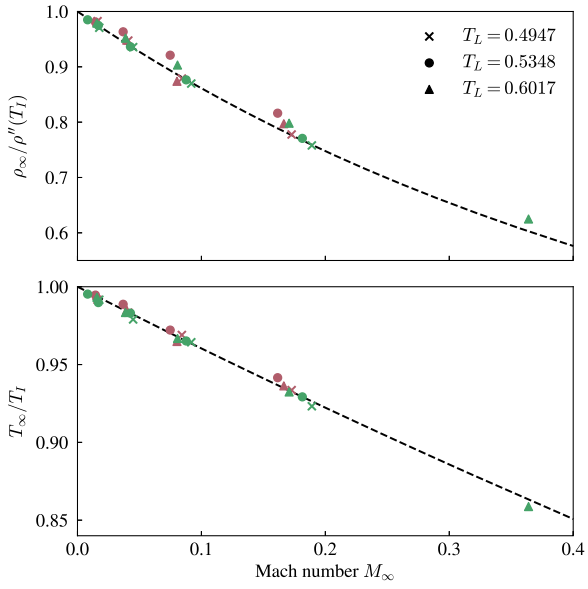

Fig. 11. Normalized density jump $\rho_\infty/\rho''(T_I)$ (top) and temperature jump T_∞/T_I (bottom) as a function of the downstream Mach number M_∞ from MD (green) and EV-DSMC (red) are compared to ideal gas kinetic theory (dashed line). (For interpretation of the references to color in this figure legend, the reader is referred to the web version of this article.)

Therein, the speed ratio $S_\infty = v_\infty/\sqrt{2RT_\infty}$ with $R = k_B/m$ is proportional to M_∞. The functions F and G are defined as

$$F(S_\infty) = -\sqrt{\pi} S_\infty \left[1 - \mathrm{erf}(S_\infty)\right] + \exp\left(-S_\infty^2\right), \tag{23}$$

$$G(S_\infty) = (2S_\infty^2 + 1)\left[1 - \mathrm{erf}(S_\infty)\right] - \frac{2S_\infty}{\sqrt{\pi}} \exp\left(-S_\infty^2\right). \tag{24}$$

Eqs. are based on an approximate, but accurate [66] moments method solution of the Boltzmann equation, combined with an *ad hoc* form of the vapor distribution function.

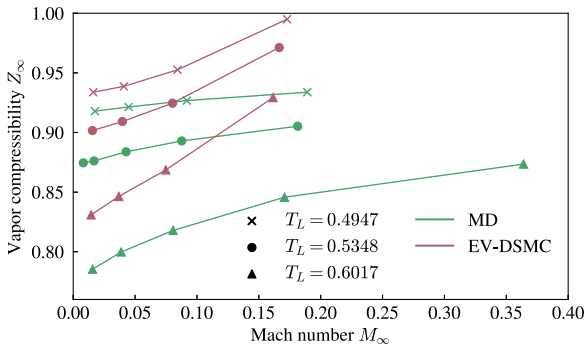

Fig. 12. MD and EV-DSMC vapor compressibility in the far field Z_∞ for a varying bulk liquid temperature T_L as a function of the downstream Mach number M_∞.

MD and EV-DSMC simulations refer to the same bulk liquid temperatures $T_L = 0.4947$, 0.5348 and 0.6017. The deviation from the ideality of the downstream vapor condition can be seen in Fig. 12. As expected for both fluids, the vapor compressibility in the far field $Z_\infty = p_\infty/(\rho_\infty k_B T_\infty)$ decreases when the liquid temperature T_L rises. For a given T_L, increasing M_∞ leads to a stronger vapor expansion, lower ρ_∞ and higher Z_∞. Although with different degrees for the two potential models, the flow conditions range from almost ideal to non-ideal. The deviations from ideal flow conditions do not seem to affect the density and temperature jumps appreciably. For both MD and EV-DSMC simulations, the temperature jump follows the nearly linear curve of the ideal gas with an evaporation coefficient of unity. The density jumps are also very close to the ideal gas curve, cf. Fig. 11. However, both MD and EV-DSMC data show slight deviations at the highest bulk liquid temperature T_L, where points exceed the jump in the ideal gas density.

A good agreement between MD, EV-DSMC and kinetic theory jumps was found, despite the different vapor–liquid interface structure of the LJ and Sutherland fluid. Jump relationships reflect the way how vapor molecules are back-scattered or absorbed by the vapor–liquid interface and the way liquid phase molecules evaporate. The good agreement suggests that in both models, the evaporation coefficient is close to unity, i.e., most of the vapor molecules hitting the interface are absorbed and liquid phase molecules enter the vapor region with a half-range Maxwellian distribution which is characterized by the saturated vapor density at the interface temperature.

4. Conclusions

The present study compared MD with EV-DSMC simulations focusing on two different scenarios under non-equilibrium conditions which comprised a vapor–liquid interface, where macroscopic quantities exhibit variations on the molecular size scale. The MD simulation method rested on the LJTS potential, while EV-DSMC simulations were conducted with the Sutherland potential. Since these two potentials are structurally different, a transformation between them was derived which accurately matches the VLE behavior of the two fluids defined by these potentials. The two non-equilibrium scenarios were used to assess the performance of both methods across a wide range of driving forces with a focus on the vapor–liquid interface. In the heat flux scenario, a closed system with a temperature gradient between bulk liquid and vapor far field was investigated, while in the other scenario classical evaporation into a half-space was considered, with a net particle flux, but zero heat flux in the vapor.

In the heat flux scenario, MD and EV-DSMC simulations showed a good agreement in the liquid and vapor phases, particularly with respect to density and temperature. However, there was a notable difference in the interfacial region. The interface thickness from EV-DSMC was consistently smaller than that obtained with MD for all considered

temperatures and driving forces. This thinner interface from EV-DSMC led to a shift of the temperature profile in the vapor phase, while its slope agreed well. Despite this difference, the overall agreement of the methods with respect to the heat flux was good.

In the evaporation scenario, the agreement of MD and EV-DSMC simulations was similar. Density and temperature in the bulk liquid and vapor phases agreed well, but the EV-DSMC simulations consistently yielded a thinner interface region. Nevertheless, the pressure in the far field of the vapor, the particle flux and the hydrodynamic velocity from the two simulation methods matched well.

The present work also investigated density and temperature jumps across the interface. For the heat flux scenario, both MD and EV-DSMC produced similar results with an overall good agreement. Small deviations between the ideal gas DSMC calculations and the MD simulations were observed for the highest temperature combined with strong gradients. This can be attributed to the DSMC simulations, which model the vapor as an ideal gas, which does not fully hold at high temperatures and in the vicinity of the interface. In the evaporation scenario, the normalized temperature and density jumps from MD and EV-DSMC matched rather well with the predictions of the kinetic theory of ideal gases assuming an evaporation coefficient of unity.

CRediT authorship contribution statement

Simon Homes: Writing – review & editing, Writing – original draft, Visualization, Validation, Supervision, Software, Resources, Project administration, Methodology, Investigation, Formal analysis, Data curation, Conceptualization. **Aldo Frezzotti:** Writing – review & editing, Writing – original draft, Visualization, Validation, Software, Resources, Methodology, Investigation, Formal analysis, Data curation, Conceptualization. **Isabel Nitzke:** Writing – review & editing, Writing – original draft, Visualization, Validation, Software, Methodology, Investigation, Formal analysis, Data curation. **Henning Struchtrup:** Writing – review & editing, Writing – original draft, Validation, Methodology, Investigation, Formal analysis, Data curation, Conceptualization. **Jadran Vrabec:** Writing – review & editing, Writing – original draft, Visualization, Validation, Supervision, Resources, Project administration, Methodology, Investigation, Funding acquisition, Formal analysis, Conceptualization.

Declaration of competing interest

The authors declare that they have no known competing financial interests or personal relationships that could have appeared to influence the work reported in this paper.

Acknowledgments

The present work in the scope of the project *MaST (Macro/Micro-simulation of Phase Decomposition in the Transcritical Regime)* was funded by *dtec.bw - Digitalization and Technology Research Center of the Bundeswehr* which the authors S.H., I.N. and J.V. gratefully acknowledge. *dtec.bw* is funded by the European Union - NextGenerationEU. The MD simulations were performed on the national supercomputer *HPE Apollo (Hawk)* at the *High-Performance Computing Center Stuttgart (HLRS)* in the scope of the project *MMHBF2* as well as on the cluster *Noctua2* at the *Paderborn Center for Parallel Computing (PC2)*. H.S. gratefully acknowledges support from the *Natural Sciences and Engineering Research Council of Canada (NSERC)* through Discovery Grant RGPIN-2022-03188.

Appendix A. Supplementary data

See supplementary material for a list of symbols as well as additional figures on the comparison between the LJTS and Sutherland potentials. Also included are property profiles resulting from the MD and EV-DSMC simulations, covering the heat flux scenario and the evaporation scenario.

Supplementary material related to this article can be found online at https://doi.org/10.1016/j.ijheatmasstransfer.2025.126828.

Data availability

Data related to the present work are available under the DOI: 10.14279/depositonce-21982.

References

[1] M. Heinen, J. Vrabec, Evaporation sampled by stationary molecular dynamics simulation, J. Chem. Phys. 151 (4) (2019) 044704, http://dx.doi.org/10.1063/1.5111759.

[2] S. Homes, M. Heinen, J. Vrabec, J. Fischer, Evaporation driven by conductive heat transport, Mol. Phys. 119 (15–16) (2021) e1836410, http://dx.doi.org/10.1080/00268976.2020.1836410.

[3] S. Homes, M. Heinen, J. Vrabec, Influence of molecular anisotropy and quadrupolar moment on evaporation, Phys. Fluids 35 (5) (2023) 052111, http://dx.doi.org/10.1063/5.0147306.

[4] S. Homes, J. Vrabec, Resistivities across the vapor–liquid interface of a simple fluid: An assessment of methods, Phys. Fluids 36 (2) (2024) 022122, http://dx.doi.org/10.1063/5.0193522.

[5] A. Frezzotti, A particle scheme for the numerical solution of the enskog equation, Phys. Fluids 9 (5) (1997) 1329–1335, http://dx.doi.org/10.1063/1.869247.

[6] R. Meland, A. Frezzotti, T. Ytrehus, B. Hafskjold, Nonequilibrium molecular-dynamics simulation of net evaporation and net condensation, and evaluation of the gas-kinetic boundary condition at the interphase, Phys. Fluids 16 (2) (2004) 223–243, http://dx.doi.org/10.1063/1.1630797.

[7] A. Frezzotti, L. Gibelli, S. Lorenzani, Mean field kinetic theory description of evaporation of a fluid into vacuum, Phys. Fluids 17 (1) (2005) 012102, http://dx.doi.org/10.1063/1.1824111.

[8] A. Frezzotti, P. Barbante, L. Gibelli, Direct simulation Monte Carlo applications to liquid-vapor flows, Phys. Fluids 31 (6) (2019) 062103, http://dx.doi.org/10.1063/1.5097738.

[9] H. Struchtrup, H. Jahandideh, A. Couteau, A. Frezzotti, Heat transfer and evaporation processes from the Enskog-Vlasov equation and its moment equations, Int. J. Heat Mass Transfer 223 (2024) 125238, http://dx.doi.org/10.1016/j.ijheatmasstransfer.2024.125238.

[10] S. Kjelstrup, D. Bedeaux, Non-equilibrium of thermodynamics of heterogeneous systems, in: Series on advances in statistical mechanics, World Scientific Publishing, Singapore, 2008, http://dx.doi.org/10.1142/9789812779144.

[11] D.C. Venerus, H.C. Öttinger, A modern course in transport phenomena, Cambridge University Press, Cambridge, 2018.

[12] Y.-P. Pao, Application of kinetic theory to the problem of evaporation and condensation, Phys. Fluids 14 (2) (1971) 306–312, http://dx.doi.org/10.1063/1.1693429.

[13] Y.-P. Pao, Temperature and density jumps in the kinetic theory of gases and vapors, Phys. Fluids 14 (7) (1971) 1340–1346, http://dx.doi.org/10.1063/1.1693612.

[14] J.W. Cipolla, H. Lang, S.K. Loyalka, Kinetic theory of condensation and evaporation. II, J. Chem. Phys. 61 (1) (1974) 69–77, http://dx.doi.org/10.1063/1.1681672.

[15] Y. Sone, Y. Onishi, Kinetic theory of evaporation and condensation - hydrodynamic equation and slip boundary condition, J. Phys. Soc. Japan 44 (6) (1978) 1981–1994, http://dx.doi.org/10.1143/jpsj.44.1981.

[16] M. Bond, H. Struchtrup, Mean evaporation and condensation coefficients based on energy dependent condensation probability, Phys. Rev. E 70 (6) (2004) 061605, http://dx.doi.org/10.1103/physreve.70.061605.

[17] I.W. Eames, N.J. Marr, H. Sabir, The evaporation coefficient of water: A review, Int. J. Heat Mass Transfer 40 (12) (1997) 2963–2973, http://dx.doi.org/10.1016/s0017-9310(96)00339-0.

[18] R. Marek, J. Straub, Analysis of the evaporation coefficient and the condensation coefficient of water, Int. J. Heat Mass Transfer 44 (1) (2001) 39–53, http://dx.doi.org/10.1016/s0017-9310(00)00086-7.

[19] H. Struchtrup, S. Kjelstrup, D. Bedeaux, Temperature-difference-driven mass transfer through the vapor from a cold to a warm liquid, Phys. Rev. E 85 (6) (2012) 061201, http://dx.doi.org/10.1103/physreve.85.061201.

[20] G. Fang, C.A. Ward, Temperature measured close to the interface of an evaporating liquid, Phys. Rev. E 59 (1) (1999) 417–428, http://dx.doi.org/10.1103/physreve.59.417.

[21] C.A. Ward, D. Stanga, Interfacial conditions during evaporation or condensation of water, Phys. Rev. E 64 (5) (2001) 051509, http://dx.doi.org/10.1103/physreve.64.051509.

[22] A.H. Persad, C.A. Ward, Expressions for the evaporation and condensation coefficients in the Hertz-Knudsen relation, Chem. Rev. 116 (14) (2016) 7727–7767, http://dx.doi.org/10.1021/acs.chemrev.5b00511.

[23] M.A. Kazemi, C.A. Ward, Assessment of the statistical rate theory expression for evaporation mass flux, Int. J. Heat Mass Transfer 179 (2021) 121709, http://dx.doi.org/10.1016/j.ijheatmasstransfer.2021.121709.

[24] V.K. Badam, V. Kumar, F. Durst, K. Danov, Experimental and theoretical investigations on interfacial temperature jumps during evaporation, Exp. Therm. Fluid Sci. 32 (1) (2007) 276–292, http://dx.doi.org/10.1016/j.expthermflusci.2007.04.006.
[25] M.T. Rauter, A. Aasen, S. Kjelstrup, Ø. Wilhelmsen, A comparative study of experiments and theories on steady-state evaporation of water, Chem. Thermodyn. Therm. Anal. 8 (2022) 100091, http://dx.doi.org/10.1016/j.ctta.2022.100091.
[26] J. Xu, S. Kjelstrup, D. Bedeaux, A. Røsjorde, L. Rekvig, Verification of Onsagers reciprocal relations for evaporation and condensation using non-equilibrium molecular dynamics, J. Colloid Interface Sci. 299 (1) (2006) 452–463, http://dx.doi.org/10.1016/j.jcis.2006.01.043.
[27] J. Ge, S. Kjelstrup, D. Bedeaux, J.M. Simon, B. Rousseau, Transfer coefficients for evaporation of a system with a Lennard-Jones long-range spline potential, Phys. Rev. E 75 (6) (2007) 061604, http://dx.doi.org/10.1103/physreve.75.061604.
[28] S.R. de Groot, P. Mazur, Non-equilibrium thermodynamics, Dover Publications, Mineola, 1984.
[29] J.P. Caputa, H. Struchtrup, Interface model for non-equilibrium evaporation, Phys. A 390 (1) (2011) 31–42, http://dx.doi.org/10.1016/j.physa.2010.09.019.
[30] H. Struchtrup, H.C. Öttinger, Nonequilibrium liquid-vapor interfaces: Linear and nonlinear descriptions, Phys. Rev. E 108 (6) (2023) 064801, http://dx.doi.org/10.1103/physreve.108.064801.
[31] L.d. Sobrino, On the kinetic theory of a van der Waals gas, Can. J. Phys. 45 (2) (1967) 363–385, http://dx.doi.org/10.1139/p67-035.
[32] M. Grmela, Kinetic equation approach to phase transitions, J. Stat. Phys. 3 (3) (1971) 347–364, http://dx.doi.org/10.1007/bf01011389.
[33] D. Enskog, The numerical calculation of phenomena in fairly dense gases, Ark. För Mat. Astron. Och Fys. 16 (1) (1921) 1–60.
[34] W. Sutherland, LII. The viscosity of gases and molecular force, Lond. Edinb. Dublin Philos. Mag. J. Sci. 36 (223) (1893) 507–531, http://dx.doi.org/10.1080/14786449308620508.
[35] J. Karkheck, G. Stell, Kinetic mean-field theories, J. Chem. Phys. 75 (3) (1981) 1475–1487, http://dx.doi.org/10.1063/1.442154.
[36] A.A. Vlasov, Many-particle theory and its application to plasma, Gordon and Breach, London, 1961.
[37] H. Struchtrup, A. Frezzotti, Twenty-six moment equations for the Enskog-Vlasov equation, J. Fluid Mech. 940 (2022) A40, http://dx.doi.org/10.1017/jfm.2022.98.
[38] A. Frezzotti, Molecular dynamics and Enskog theory calculation of shock profiles in a dense hard sphere gas, Comput. Math. Appl. 35 (1) (1998) 103–112, http://dx.doi.org/10.1016/s0898-1221(97)00261-7.
[39] Y. Sone, Kinetic theoretical studies of the half-space problem of evaporation and condensation, Transport Theory Statist. Phys. 29 (3–5) (2000) 227–260.
[40] T. Ytrehus, Molecular-flow effects in evaporation and condensation at interfaces, Multiph. Sci. Technol. 9 (3) (1997) 205–327, http://dx.doi.org/10.1615/multscientechn.v9.i3.10.
[41] C. Cercignani, The Boltzmann equation and its applications, Springer, Heidelberg, 1988, http://dx.doi.org/10.1007/978-1-4612-1039-9.
[42] C. Niethammer, S. Becker, M. Bernreuther, M. Buchholz, W. Eckhardt, A. Heinecke, S. Werth, H.-J. Bungartz, C.W. Glass, H. Hasse, J. Vrabec, M. Horsch, ls1 mardyn: The massively parallel molecular dynamics code for large systems, J. Chem. Theory Comput. 10 (10) (2014) 4455–4464, http://dx.doi.org/10.1021/ct500169q.
[43] G. Rutkai, M. Thol, R. Span, J. Vrabec, How well does the Lennard-Jones potential represent the thermodynamic properties of noble gases? Mol. Phys. 115 (9–12) (2016) 1104–1121, http://dx.doi.org/10.1080/00268976.2016.1246760.
[44] J.E. Jones, On the determination of molecular fields. - i. From the variation of the viscosity of a gas with temperature, Proc. R. Soc. Lond. A 106 (738) (1924) 441–462, http://dx.doi.org/10.1098/rspa.1924.0081.
[45] J.E. Jones, On the determination of molecular fields. - II. From the equation of state of a gas, Proc. R. Soc. Lond. A 106 (738) (1924) 463–477, http://dx.doi.org/10.1098/rspa.1924.0082.
[46] M. Thol, G. Rutkai, R. Span, J. Vrabec, R. Lustig, Equation of state for the Lennard-Jones truncated and shifted model fluid, Int. J. Thermophys. 36 (1) (2015) 25–43, http://dx.doi.org/10.1007/s10765-014-1764-4.
[47] J. Vrabec, G.K. Kedia, G. Fuchs, H. Hasse, Comprehensive study of the vapour-liquid coexistence of the truncated and shifted Lennard-Jones fluid including planar and spherical interface properties, Mol. Phys. 104 (9) (2006) 1509–1527, http://dx.doi.org/10.1080/00268970600556774.
[48] M. Heier, S. Stephan, J. Liu, W.G. Chapman, H. Hasse, K. Langenbach, Equation of state for the Lennard-Jones truncated and shifted fluid with a cut-off radius of 2.5 sigma based on perturbation theory and its applications to interfacial thermodynamics, Mol. Phys. 116 (15–16) (2018) 2083–2094, http://dx.doi.org/10.1080/00268976.2018.1447153.
[49] M.P. Lautenschlaeger, H. Hasse, Transport properties of the Lennard-Jones truncated and shifted fluid from non-equilibrium molecular dynamics simulations, Fluid Phase Equilib. 482 (2019) 38–47, http://dx.doi.org/10.1016/j.fluid.2018.10.019.
[50] D. Enskog, Kinetische theorie der wärmeleitung, reibung und selbstdiffusion in gewissen verdichteten gasen und flüssigkeiten, K. Sven. Vetenskapsakademiens Handl. 63 (1922) 1–44.
[51] P. Resibois, M. DeLeener, Classical kinetic theory of fluids, J. Wiley & Sons, New York, 1977.
[52] H. van Beijeren, M.H. Ernst, The modified enskog equation, Physica 68 (1973) 437–456, http://dx.doi.org/10.1016/0031-8914(73)90372-8.
[53] N.F. Carnahan, K.E. Starling, Equation of state for nonattracting rigid spheres, J. Chem. Phys. 51 (2) (1969) 635–636, http://dx.doi.org/10.1063/1.1672048.
[54] R. Balescu, Equilibrium and Nonequilibrium Statistical Mechanics, John Wiley & Sons, New York, 1975.
[55] G.A. Bird, Molecular gas dynamics and the direct simulation of gas flows, Clarendon Press, Oxford, 1994, http://dx.doi.org/10.1093/oso/9780198561958.001.0001.
[56] M.P. Allen, D.J. Tildesley, Computer simulation of liquids, Oxford University Press, Oxford, 2017, http://dx.doi.org/10.1093/oso/9780198803195.001.0001.
[57] M.D. Arthur, C. Cercignani, Non-existence of a steady rarefied supersonic flow in a half-space, Z. Für Angew. Math. Und Phys. 31 (5) (1980) 634–645, http://dx.doi.org/10.1007/bf01596163.
[58] Y. Tang, Role of the Barker–Henderson diameter in thermodynamics, J. Chem. Phys. 116 (15) (2002) 6694–6700, http://dx.doi.org/10.1063/1.1461360.
[59] C. Cercignani, Strong evaporation of a polyatomic gas, in: Rarefied Gas Dynamics; International Symposium, 12th, Charlottesville, VA, July 7-11, 1980, Technical Papers, Part 1, American Institute of Aeronautics and Astronautics, New York, 1981, pp. 305–320.
[60] T. Tsuruta, H. Tanaka, T. Masuoka, Condensation/evaporation coefficient and velocity distribution at liquid-vapor interface, Int. J. Heat Mass Transfer 42 (1999) 4107–4116, http://dx.doi.org/10.1016/s0017-9310(99)00081-2.
[61] S. Fujikawa, T. Yano, M. Watanabe, Vapor-Liquid Interfaces, Bubbles and Droplets, Springer, Heidelberg, 2011, http://dx.doi.org/10.1007/978-3-642-18038-5.
[62] F. Sharipov, Data on the velocity slip and temperature jump on a gas-solid interface, J. Phys. Chem. Ref. Data 40 (2) (2011) 023101, http://dx.doi.org/10.1063/1.3580290.
[63] S. Chapman, T.G. Cowling, The Mathematical Theory of Non-Uniform Gases, Cambridge University Press, Cambridge, 1990.
[64] G. Galliéro, C. Boned, A. Baylaucq, Molecular dynamics study of the Lennard-Jones fluid viscosity: Application to real fluids, Ind. Eng. Chem. Res. 44 (17) (2005) 6963–6972, http://dx.doi.org/10.1021/ie050154t.
[65] P. Barbante, A. Frezzotti, A comparison of models for the evaporation of the Lennard-Jones fluid, Eur. J. Mech. B Fluids 64 (2017) 69–80.
[66] A. Frezzotti, A numerical investigation of the steady evaporation of a polyatomic gas, Eur. J. Mech. B 26 (1) (2007) 93–104, http://dx.doi.org/10.1016/j.euromechflu.2006.03.007.